Research Article

Valérie Van Grootel*, Marie-Julie Péters, Elizabeth M. Green, Stéphane Charpinet, Pierre Brassard, and Gilles Fontaine

New observations and asteroseismic analysis of the subdwarf B pulsator PG 1219+534

https://doi.org/10.1515/astro-2018-0014
Received Sep 30, 2017; accepted Dec 26, 2017

Abstract: We present a new asteroseismic modeling of the hot B subdwarf (sdB) pulsator PG 1219+534, based on a 3-month campaign with the Mont4K/Kuiper combination at Mt Bigelow (Arizona) and on updated atmospheric parameters from high S/N low and medium resolution spectroscopy. On the basis of the nine independent pulsation periods extracted from the photometric light curve, we carried out an astroseismic analysis by applying the forward modeling approach using our latest (third and fourth generation) sdB models. Atmospheric parameters ($T_{\rm eff}$ = 34 258 ± 170 K, $\log g$ = 5.838 ± 0.030) were used as independent constraints, as well as partial mode identification based on observed multiplet structures we ascribed to stellar rotation. The optimal model found is remarkably consistent between various analyses with third and fourth generation of sdB models, and also with previously published analysis with second generation sdB models. It corresponds to a sdB with a canonical mass (0.46 ± 0.02 $M_{\odot}$), rather thin H-He envelope (log q(envl) = −3.75 ± 0.12), and close to He-burning exhaustion ($X_{\rm core}(C+O)$ = 0.86 ± 0.05). We also investigate the internal rotation of the star. We find that PG 1219+534 rotates very slowly ($P_{\rm rot}$ = 34.91 ± 0.84 days) and that solid-body rotation is reached at least down to ∼60% of the radius.

Keywords: subdwarfs, stars: oscillation, stars:interior, stars: individual: PG 1219+534

1 Introduction

Subdwarf B (sdB) stars and related objects harbour various classes of pulsators. The two main classes are the short-period (80–600 s) pulsators (called the EC14026, V361Hya, or sdBV$_{\rm r}$ class), and the long-period (30 min–3h) pulsators (called PG1716, V1093 Her, or sdBV$_{\rm s}$ class). The short-period pulsations usually correspond to low-order p-modes, while long-period pulsations are generally mid- to high-order g-modes. Many sdB pulsators are actually hybrid pulsators (as revealed by *Kepler*), with predominantly short-period oscillations, or predominantly long-period oscillations. The oscillations are produced by the κ-mechanism related to the opacity of heavy elements, mainly iron. Local iron overabundances are indeed present in the stellar envelope, if we consider microscopic diffusion with an equilibrium between gravitational settling and radiative levitation (Charpinet et al. 1996, 1997; Fontaine et al. 2003).

PG 1219+534 is one of the very first sdB rapid pulsators discovered (Koen et al. 1999), with 4 pulsations in the range 129–148 s. A subsequent 4-night campaign at Canada-France-Hawaii Telescope (CFHT) identified 9 independent pulsation periods in the range 122–172 s (Charpinet et al. 2005). These observations were the base of the first asteroseismic modeling of PG 1219+534, using the second-generation (2G; Charpinet et al. 1997) models for sdB stars. In the present study, we improve the overall quality of the asteroseismic analysis, by gathering new spectroscopic and photometric observations including a 3-month high time resolution campaign carried out with the Mont4k instrument at the 1.6-m Kuiper telescope at Mt Bigelow (Arizona), and by using more sophisticated models (third and fourth generation, i.e. 3G and 4G). These 3G

Corresponding Author: Valérie Van Grootel: Space sciences, Technologies, and Astrophysics Research (STAR) Institute, Liège University, 19C Allée du six-aout, B-4000 Liège, Belgium;
Email: valerie.vangrootel@uliege.be
Marie-Julie Péters: Space sciences, Technologies, and Astrophysics Research (STAR) Institute, Liège University, 19C Allée du six-aout, B-4000 Liège, Belgium
Elizabeth M. Green: Steward Observatory, University of Arizona, 933 North Cherry Avenue, Tucson, AZ, 85721, United States of America
Stéphane Charpinet: Université de Toulouse, UPS-OMP, IRAP, 14 Avenue Edouard Belin, F-31400 Toulouse, France
Pierre Brassard, Gilles Fontaine: Département de Physique, Université de Montréal, CP 6128, Succursale Centre-Ville, Montréal, QC H3C 3J7, Canada

models were presented in detail in Van Grootel et al. (2013), while it is the first time here in this paper that the 4G models are described and applied.

This paper is organized as follows. In Sect. 2, we describe the new observations and the Fourier analysis to extract oscillation properties. In Sect. 3, we present the models and methods for asteroseismic analysis, which is carried out on Sect. 4. We also compare there the results from various seismic models, and obtain the rotation properties of PG 1219+534. We conclude in Sect. 5.

2 Observations

2.1 Updated spectroscopic estimates for PG1219+534

A detailed atmospheric analysis of PG 1219+534 is presented in Charpinet et al. (2005), from mid-resolution MMT and low-resolution Bok telescope spectra. These spectra were analyzed with our NLTE, metal-free sdB model atmospheres, giving atmospheric parameters $T_{\rm eff}$ = 33 600 ± 370 K, $\log g$ = 5.810 ± 0.046, and $\log N({\rm He})/N({\rm H})$ = −1.49 ± 0.08 (all quoted uncertainties for spectroscopic estimates are formal errors of the fit only). As part of our Tucson-Montréal global program aimed at improving the spectroscopic characterization of sdB stars, we gathered over the years further mid- and low-resolution spectra of PG 1219+534 with Steward Observatory's 2.3-m Bok telescope and the 6.5-m MMT, both in Arizona. Compared to Charpinet et al. (2005), we have now developed the capacity to build NLTE model atmospheres and synthetic spectra with arbitrary heavy element abundances for a wide range of H and He compositions within reasonable computation times. We derived from the results of Blanchette et al. (2008), a representative composition using the most abundant heavy elements. Hence, we assumed atmospheres containing C (1/10 solar), N (solar), O (1/10 solar), Si (1/10 solar), S (solar), and Fe (solar).

Figure 1 shows the results of our best fits, with model atmospheres including metals in the above proportions. We took the mean of the three results to obtain our updated estimates for the atmospheric parameters of PG 1219+534: $T_{\rm eff}$ = 34 258 ± 170 K, $\log g$ = 5.838 ± 0.030, and $\log N({\rm He})/N({\rm H}) = -1.475 \pm 0.030$. To provide a measure of the uncertainties associated with the presence (or the absence) of metals, we refitted our spectrum with NLTE atmosphere models containing only H and He. We found $T_{\rm eff}$ = 33 824 ± 137 K, $\log g = 5.824 \pm 0.028$, and $\log N({\rm He})/N({\rm H}) = -1.479 \pm 0.028$, thus indicating that the presence of metals is not a critical issue in determining the atmospheric parameters of PG 1219+534.

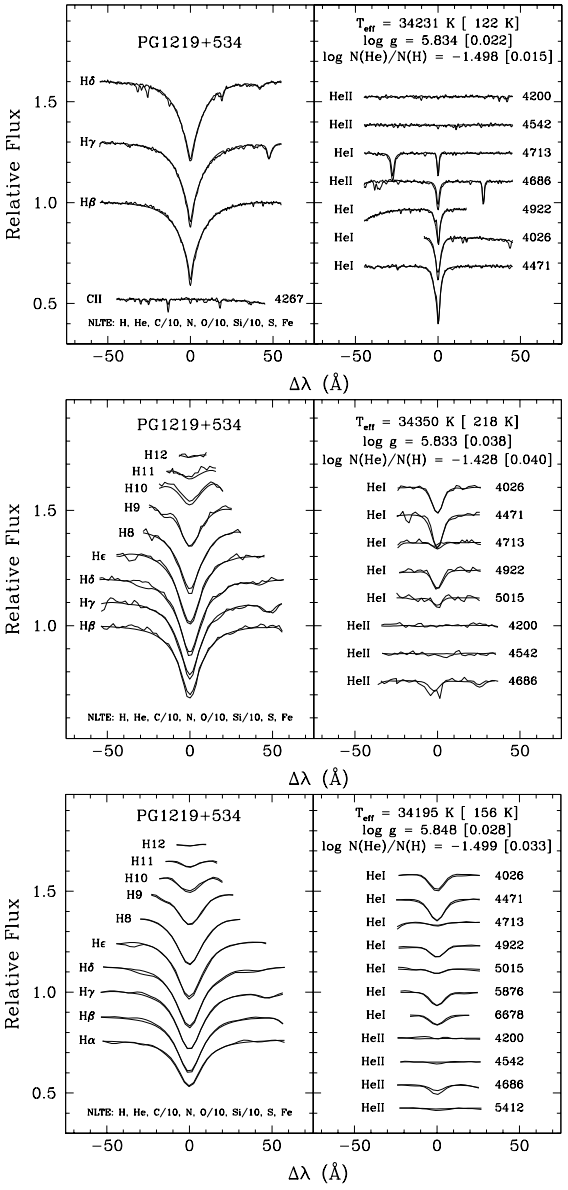

Figure 1. *Top panel:* Model fit (solid curves) to all the hydrogen and helium lines available in our moderately high S/N, 1A resolution MMT optical spectra of PG 1219+534. The fit was done using a three-dimensional grid of NLTE synthetic spectra ($T_{\rm eff}$, $\log g$, $\log N({\rm He})/N({\rm H})$ in which the abundances of C, N, O, S, Si, and Fe were fixed at amounts consistent with Blanchette et al. (2008). *Middle panel:* Same, but for our high S/N 6A resolution Bok telescope spectra. *Low panel:* Same, but for high S/N 9A resolution Bok telescope spectra.

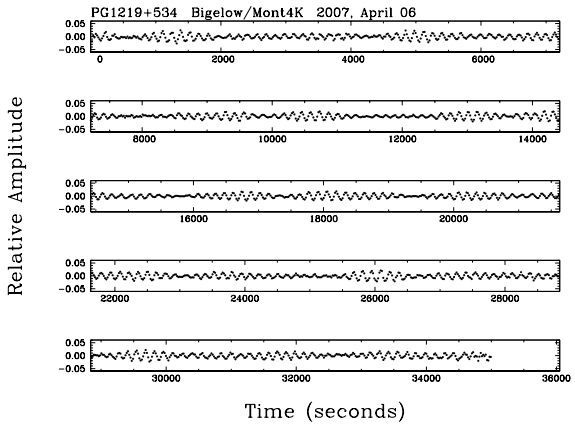

Figure 2. Expanded view of the light curve obtained on 6 April 2007 in units of fractional brightness intensity and seconds.

2.2 New photometric observations

We gathered from February 3 to May 3, 2007, high quality photometric data with the Mont4K CCD imager installed on Steward Observatory's 1.55-m Mt. Bigelow telescope in Arizona. We obtained 198.7 h of data, achieving a duty cycle of 9.3%. The formal resolution of the campaign is 0.13 μHz, and the noise level is 0.004%. The remarkable quality of the photometry can be fully appreciated from the expanded view of a single (6 April 2007) night's light curve proposed in Figure 2. The relative noise level is similar of that achieved on much larger telescopes.

2.3 Fourier analysis

To extract the frequencies, a Fourier analysis and pre-whitening techniques were applied to the total light curve resulting from the combination of individual nights. We used our dedicated software FELIX (Frequency Extraction for LIghtcurve eXploitation; Charpinet et al. 2011) that greatly eases and accelerates the application of this procedure. The pre-whitening technique consists of subtracting frequencies of the pulsation spectrum one by one in the time domain. At each step, the Fourier transform of the residual light is computed and the procedure is reapplied until the amplitude of the peaks in the Fourier domain gets below the threshold of $\sim$4 times the noise level. The Fourier transform of the light curve and the residual following from the steps of pre-whitening sequence are illustrated in Figure 3. The multiple peaks confirm the presence of multiperiodic oscillations in the light curve. Most oscillation modes are found in the 5 – 15 mHz range, and the dominant peak is located close to 7 mHz. Some low-amplitude peaks are also present in the 50–200 μHz range, in the domain of g-modes oscillations. The daily alias at 11.6 μHz and some of its harmonics are also clearly visible (Figure 3, top right panel).

Table 1 presents the practical list of oscillation modes that will be used in our seismic analysis. We have excluded the marginal periods below the detection threshold and the harmonic of the dominants periods, considering only the secured oscillation modes, above S/N = 4.5[1]. We note in particular four multiplet structures around f_{016} (triplet), f_{002} (triplet), f_{003} (triplet), and f_{041} (doublet). A similar spacing is present in the f_{003} triplet and in the f_{041} doublet that is around 0.30 μHz, while the spacing in the f_{002} triplet is close to twice this value, at around 0.62 μHz. The triplet structure in the g-mode regime is about 0.52 μHz, potentially reconciliable with spacing of p-modes if we consider a Ledoux coefficient of 0.16, as for $l = 2$ modes. This suggests that these multiplet structures are most likely associated with rotational splitting. We will explore this hypothesis in Sect. 4. We also provide for comparison in Table 1 the oscillation modes present in the discovery campaign of Koen et al. (1999), as well as those detected at CFHT and used by Charpinet et al. (2005). No splitting was identified and one of the periods that we will use (f_{056}) was below the noise limit. Another pulsation mode (at 122.408s, labelled $f_{\rm CFHT}$) was identified only in CFHT. We finally note that a pulsation mode with a 135.2s period (labelled $f_{\rm noise}$ in Table 1) was detected both at CFHT and at Mt Bigelow, but is below the detection threshold in both cases.

3 Models and methods for asteroseismic analysis

The 3G models are static (parameterized) structures representing the star from the surface to its center, contrary to the 2G models that are missing the innermost regions. These models are constructed assuming hydrostatic and thermal equilibrium, and are defined by a given set of model parameters, including the size and chemical composition of the core. They allow for the computation of accurate periods/frequencies for p-modes and g-modes (including possible mixed modes), while the former generation of envelope models was limited to the p-modes in terms of accuracy. Third generation models were pre-

1 We also considered the isolated f_{056} mode at S/N=4.3 as reliable.

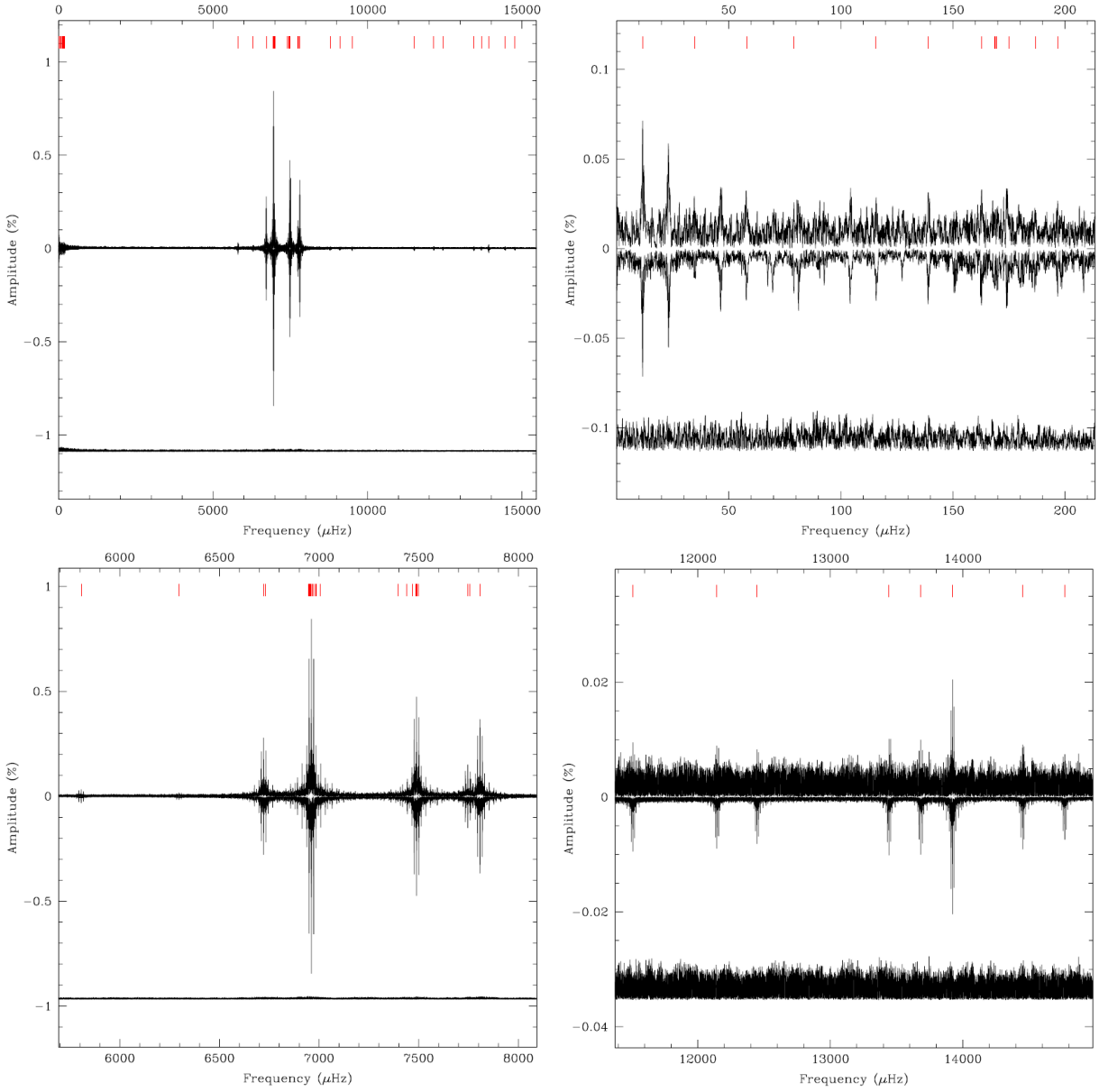

Figure 3. Fourier Transforms (FT) of the entire data set in the 0–15 mHz frequency range (*top left panel*), in the 0–210 mHz (*top right*), in the 5700–8000 mHz (*bottom left*) and in the 11 700–14 500 mHz frequency range (*bottom right*). In all panels the up FT is the observed full spectrum, while the reverse FT is the model spectrum reconstructed on the basis of the pulsations extracted from the light curve. The curve shifted downward is the point-by-point difference between the actual FT and the model FT.

sented in detail in Van Grootel et al. (2013), who also provided a test of accuracy of these models performed with the pulsating eclipsing binary PG1336-018. By comparing the results of orbital modeling and asteroseismology, it was possible to show the strong reliability of the 3G models to derive global stellar parameters, in particular for the mass of the star.

The 4G models are identical to 3G models, except for two refinements: they present a double H/He transition profile in the envelope (to take into account He diffusion), and they take into account the pollution of (whole or part of) the He-mantle by a small amount (0–7%) of C created during the He-flash. The slopes of all chemical transitions are also parameterized (as long as the star evolves, it is expected that the transition is progressively smoothed thanks to the action of diffusion), while they were usually considered fixed in previous generations of models and corresponded to steep transition profiles (they were calibrated on evolutionary sequences without diffusion). Up to 12 parameters can then be considered: the total mass

Table 1. List of oscillation modes from the combined light curve of PG 1219+534 obtained in Mt Bigelow that will be used in our asteroseismic modeling. The oscillation modes detected at CFHT and used by Charpinet et al. (2005) are also listed, as well as those of the discovery campaign of Koen et al. (1999).

Id.	Frequency (μHz)	Period (s)	Amplitude (%)	S/N	P_{CFHT04} (s)	A_{CFHT04} (%)	Comments
f_{019}	115.676	8644.832	0.0339	5.7	...	...	
f_{014}	138.892	7199.818	0.0429	7.3	...	...	
f_{011}	162.752	6144.327	0.0487	8.4	...	...	
f_{020}	168.494	5934.944	0.0333	5.7	...	...	Possible multiplet:
f_{016}	169.023	5916.360	0.0403	7.0	...	...	$\Delta\nu = f_{016} - f_{020} = 0.53$ μHz
f_{012}	169.533	5898.564	0.0448	7.8	...	...	$\Delta\nu = f_{012} - f_{016} = 0.51$ μHz
f_{018}	174.872	5718.484	0.0356	6.2	...	...	
f_{025}	187.000	5347.592	0.0293	5.1	...	...	
f_{022}	5806.54	172.220	0.0312	10.9	172.214	0.0456	
f_{041}	6297.60	158.791	0.0163	5.4	158.789	0.0334	Possible doublet:
f_{042}	6297.88	158.784	0.0160	5.5	...	...	$\Delta\nu = f_{042} - f_{041} = 0.29$ μHz
f_{004}	6721.49	148.777	0.3035	89.9	148.775	0.4053	Also in Koen et al. (1999)
f_{001}	6961.38	143.650	0.8373	229.3	143.649	0.7228	Also in Koen et al. (1999)
f_{noise}	*[7398.16]*	*[135.169]*	*[0.0147]*	3.9	[135.160]	[0.0429]	below detection threshold; not used for seismology
f_{006}	7488.83	133.532	0.2655	75.5	...	...	Possible multiplet:
f_{002}	7489.45	133.521	0.3915	111.4	133.516	0.6874	Also in Koen et al. (1999); $\Delta\nu = f_{002} - f_{006} = 0.62$ μHz
f_{005}	7490.09	133.510	0.2913	82.9	...	...	$\Delta\nu = f_{005} - f_{002} = 0.64$ μHz
f_{007}	7746.37	129.093	0.1567	47.4	...	...	
f_{030}	7807.42	128.083	0.0237	7.4	...	...	Possible multiplet:
f_{003}	7807.75	128.078	0.3745	117.0	128.077	0.7972	Also in Koen et al. (1999); $\Delta\nu = f_{003} - f_{030} = 0.33$ μHz
f_{037}	7808.06	128.073	0.0198	6.2	...	...	$\Delta\nu = f_{037} - f_{003} = 0.31$ μHz
f_{CFHT}	...	...	...		122.408	0.0963	not present in the Mt Bigelow data
f_{053}	11 511.59	86.869	0.0097	4.5	...	...	
f_{056}	12 145.32	82.336	0.0091	4.3	[82.261]	0.0190	not used by Charpinet et al. (2005)

of the star $M_\star$, the fractional mass of the H/He envelope $\log q$(envl) (often noted $\log q$(H) in our previous publications), the amount of H in this H-He envelope, the fractional mass of the upper pure-H envelope $\log q$(envl,diff), the amount of C-pollution in the He-rich mantle, the fractional mass of the C-polluted mantle $\log q$(mantle,flash), the fractional mass of the core $\log(M_{\rm core}/M_\star)$, and the chemical composition in the core (with X(He) + X(C) + X(O)=1); plus four parameters related to the slope of the four chemical transitions. These parameters are illustrated on Figure 4. PG 1219+534 is the first star on which these 4G models are applied.

The method used to interpret the oscillation spectrum of PG 1219+534 is the forward method in asteroseismology. It basically consists of comparing simultaneously the observed pulsation periods with those computed theoretically from stellar models (for details, see, *e.g.*, Charpinet et al. 2005). The a priori mode identification was complicated for sdB stars considering their weak magnitudes ($V \sim 15$ typically), so a double-optimization procedure is applied. The first optimization determines the best match between the observed periods and those calculated for a given model (eventually within partial mode identification from rotational splitting, for instance), and the second optimization searches in a given parameter space (i.e. for a specified range of stellar masses, core and envelop masses and compositions, etc.) for the models that can best reproduce the data. In practice, given that the stellar models are defined by a finite number of parameters a_i, the best fit(s) between observed periods and theoretical periods are obtained by minimizing the χ^2-type merit function

$$S^2(a_1, a_2, \ldots, a_n) = \sum_{i=1}^{N_{obs}} \left(\frac{P_{obs,i} - P_{th,i}}{\sigma_i} \right)^2 \qquad (1)$$

where N_{obs} is the number of observed periods in the star, P_{obs} is the observed periods, P_{th} is the theoretical periods and σ_i represents the weight of each pair $\{P_{obs}, P_{th}\}$. We chose $\sigma = 1$ for each of them. Based to the principle of natural selection, the genetic algorithm code LUCY has been developed to obtain an approximate solution of the global optimization problem, the closest possible to the actual optimal model, by growing a random population of po-

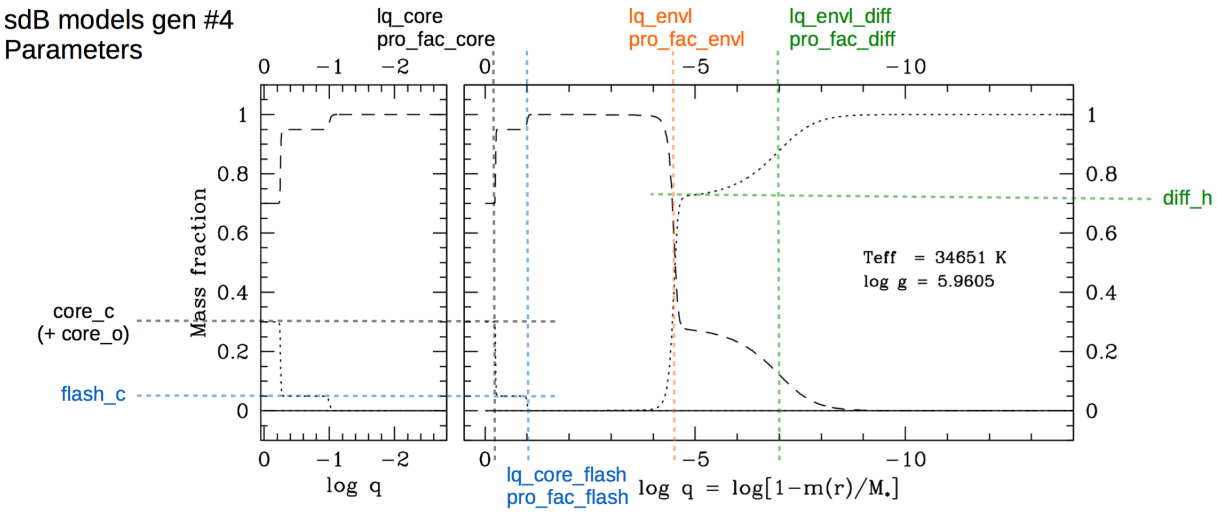

Figure 4. Parameters for the 4G sdB models.

tential solutions from generation to generation (Charpinet et al. 2008).

As for 3G models, the atmospheric parameters $T_{\rm eff}$ and $\log g$ are not input parameters of the models and are computed a posteriori for a given model. Since spectroscopic constraints are essential to guide the search for a meaningful asteroseismic solution in the vast parameter space and avoid the multiplication of inconsistent solutions, the adopted solution is to incorporate these constraints within the optimization procedure itself, by applying a correction factor to the S^2 value to the models that differ in $T_{\rm eff}$ and $\log g$ above 3σ of the spectroscopic values.

Note that the number of free parameters may become higher than the number of observed periods, particularly with 4G models (see an example in Sect. 4.2.3). The usual understanding is that the optimization problem is underdetermined if the number of model parameters is higher than the number of observed periods. However, this is true only for linear mathematical problems; our optimization is not a linear problem. In asteroseismology, the response of the pulsation periods on the variation of one of the defining parameters is highly nonlinear and mode-dependent (see, *e.g.*, Giammichele et al. 2017 for a thorough discussion on this point).

4 Asteroseismic analysis of PG 1219+534

We first only used p-modes to model PG1219+534. The nine independent modes we considered are: f_{022}, f_{042}, f_{004}, f_{001}, f_{002}, f_{007}, f_{003}, f_{053} and f_{056}. We considered all theoretical modes of degree $\ell = 0$, 1, 2 and 4 between 70 and 200 s. Those with $\ell = 3$ were explicitly excluded, having an extremely low visibility in the optical domain owing to cancellation effects because of their specific surface geometry (Randall et al. 2005). Finally, we restricted the degree of the only dominant modes (f_{001},f_{002} and f_{003}) to be $\ell \leq 2$. Indeed, the multicolor photometry carried out when possible showed that all dominant modes are identified to the degree $\ell = 0$, 1 or 2 (*e.g.* Tremblay et al. 2006; Van Grootel et al. 2008). We also required f_{002}, f_{003} and f_{041} (that exhibit multiplet structures) to be $\ell \geq 1$. We next considered also g-modes of degree $\ell = 1$, 2 between 5200 and 8800 s, for a comparison to the six independent g-modes f_{019}, f_{014}, f_{011}, f_{016}, f_{018}, f_{025}.

4.1 3G results

This 3G modeling of PG 1219+534 was the M.Sc. thesis of one of us (M.J. Péters). We searched (only for the p-modes) seismic solutions in the following space: $0.35 \leq M_*/M_\odot \leq 0.60$, $-6.0 \leq \log q(\text{envl}) \leq -2.80$, $-0.50 \leq \log q(\text{core}) \equiv \log(1 - M_{\rm core}/M_*) \leq -0.10$, $0 \leq X_{\rm core}(C+O) \equiv X_{\rm core}(C) \leq 0.99$[2], and $0.1 \leq \text{profac(envl)} \leq 30$. The constraints on $\log q$(envl) and M_* rely on expectations from stellar modeling and various formation scenarios for hot B subdwarfs (see Han et al. 2002, 2003), whereas the range for the core size is loosely inspired by horizontal branch stellar evolution calculations (Dorman et al. 1993). The parameter pro-

2 We have found that theoretical periods are not very sensitive to the exact core composition of C and O. Grouping (C+O) in one parameter facilitates and speeds up the optimization procedure.

fac(envl) ranges from a very smooth transition profile to a very steep one. We launched the optimization with typically 120 individuals and 120 generations.

Within the parameter space specified, a clear optimal model emerged. This best-fit model has $T_{\rm eff}$ = 33 850 K, $\log g$ = 5.81, $M_\star$ = $0.437 M_\odot$, $\log q$(envl) = −4.35, $\log q$(core) = −0.36, $X_{\rm core}(C+O)$ = 0.91, and pf(envl)=4.5. Figure 5 shows maps of the S^2 function around the optimal model solution in a two-parameter space, with the other parameters set to their optimal values given by the best-fit model. The left-hand panel of Figure 5 shows a slice of the S^2 hyper-surface along the $M_\star$–$\log q$(envl) plane whereas the right-hand panel shows a slice along the $\log q$(core)–$X_{\rm core}(C+O)$. This means, for the left-hand panel for example, that at each $M_\star$, $\log q$(envl) position, the value given is the projected merit function, i.e. the minimum of $\log S^2$ that can be found among the values obtained for all $\log q$(core), $X_{\rm core}(C+O)$, and pf(env). The S^2 function is given on a logarithmic scale. As shown on the right color scale, the areas of the plots filled with dark blue represent the good fits between the observed and theoretical periods. The location of the optimal model in the maps is indicated by a cross. White contours show regions where the period fits have S^2 values within 1, 2, and 3σ confidence level relative to the best-fit model. This best-fit model provides an excellent fit to the nine p-modes: average relative dispersion is $\overline{\Delta X/X} \simeq 0.35\%$, corresponding to $\overline{\Delta P} \simeq 0.37$ s on an absolute scale.

4.2 4G results

4.2.1 4G models, 5 parameters

We first used 4G models "as 3G models", with only 5 parameters ($M_\star$, $\log q$(envl), $\log q$(core), X(C+O) (here again, $\equiv X(C)$), and profac(envl). The parameter space was the same as before, but we increased the optimization to 200 individuals and 500 generations. We also used an improved version of the genetic algorithm optimization code, which we constantly develop over the years. We obtained a very similar optimal model: $T_{\rm eff}$ = 34 053 K, $\log g$ = 5.805, $M_\star$ = $0.441 M_\odot$, $\log q$(envl) = −4.35, $\log q$(core) = −0.37, $X_{\rm core}(C+O)$ = 0.92, and pf(envl) = 3.1. This model is presented in Table 2 as Model I. The average relative dispersion is $\overline{\Delta X/X} \simeq 0.38\%$, thus fully confirming the results with 3G models.

4.2.2 4G models, 8 parameters

We next considered the double H/He transition profile in the envelope, with 3 more parameters (see Figure 4): $\log q$(envl,diff) (searched between −3.0 and −10.0[3]), profac(diff) (searched between 1 and 5), and diffH (searched between 60% and 100%). We typically considered 250 individuals over 2000 generations. Two rather close models emerged, both with a best-fit improvement compared to the results with 5 parameters: $\overline{\Delta X/X} \simeq 0.16\%$. These models are presented in Table 2, as Model II and Model IIbis. They are clearly visible in Figure 6, which shows the usual maps of the S^2 function.

4.2.3 4G models, 11 parameters

Finally, we considered full 4G models, with 3 more parameters related to the potential C-pollution of the He mantle (see Figure 4): $\log q$(core, flash) (searched between -6.0 and -0.4), FlashC (0–7%), and profac(flash) (searched between 10.0 and 50.0). We carried out optimization with 400 individuals and 5000 generations. Here again, two optimal models emerged: they are listed in Table 2 as Model III and Model IIIbis. Contrary to the move from 5 to 8 parameters, the move from 8 to 11 parameters is only a marginal improvement of the merit function ($\overline{\Delta X/X} \simeq 0.13\%$). A likely explanation is that these added parameters are simply not well constrained by p-modes. It is also likely linked to the quality of the fit, which is rather good but still far from a null merit function, and the weak impact of these parameters on the computed periods (weaker than the impact of stellar mass, thickness of the envelope, etc. on computed periods) do not us allow us to constrain them. But, as underlined above, we do not think it is linked to the fact that the number of model parameters is higher than the number of observed periods, since this assertion valid for linear optimization problem do not stand on firm grounds here.

The histograms obtained for the probability density function for each of the 11 parameters are shown on Figure 7. These histograms provide more quantitative statements by statistically estimating the value for each parameter of the star and its associated error from the asteroseismic fit. They are obtained following the procedure described in Van Grootel et al. (2013), based on merit function of all models computed when exploring the parameter space during the optimization. Figure 7 shows that

3 if $\log q$(envl,diff) > $\log q$(envl), a single transition profile, as in 2G and 3G models, is considered.

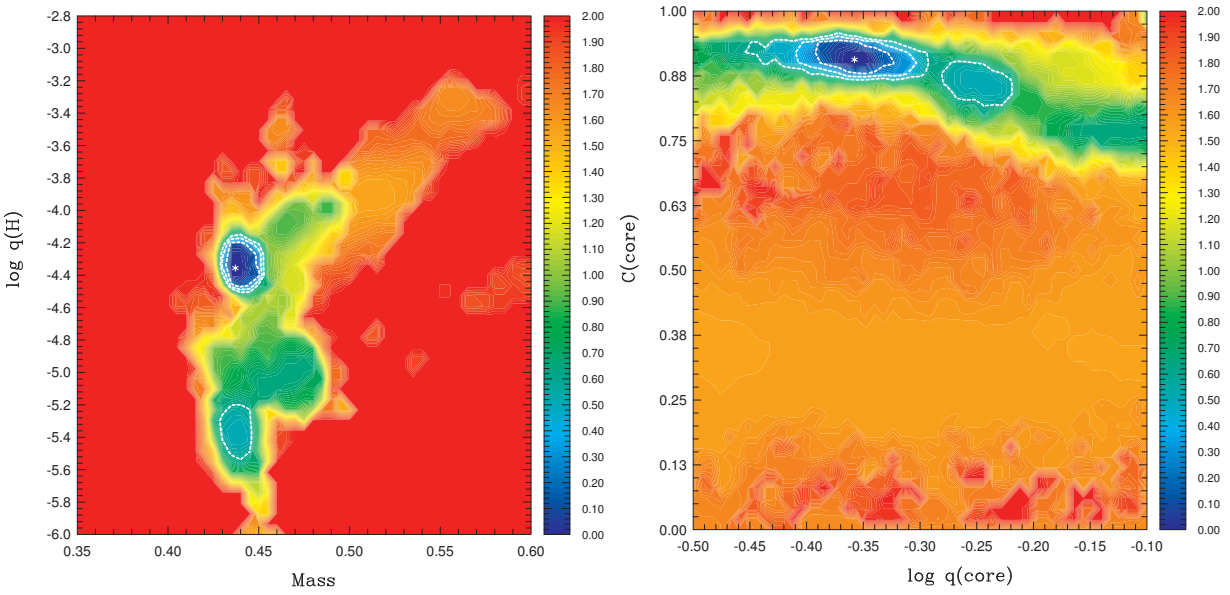

Figure 5. Optimization with 3G models. *Left panel*: Map of the projected merit function S^2 (on a logarithmic scale) in the log q(envl)–M_* plane. At each M_*, log q(envl) position, the value given is the minimum of log S^2 that can be found among the values obtained for all log q(core) and $X_{\rm core}(C+O)$. *Right panel*: Map of the projected merit function S^2 (on a logarithmic scale) in the log q(core)–$X_{core}(C+O)$ plane where the best-fit model is indicated by a star. White contours show regions where the period fits have S^2 values within the 1σ, 2σ and 3σ confidence levels relative to the best-fit solution.

Table 2. Optimal 4G models and their mode identification for the nine independent p-modes.

(Id.)	Period	l	k	l	k	l	k	l	k	l	k
f_{056}	82.336	2	6	2	6	2	6	2	6	2	6
f_{056}	86.869	1	6	1	6	1	6	1	6	1	6
f_{003}	128.078	1	3	1	3	1	3	1	3	1	3
f_{007}	129.093	4	2	4	2	4	2	4	2	4	2
f_{002}	133.521	2	2	2	2	2	2	2	2	2	2
f_{001}	143.650	1	1	1	1	1	1	1	1	1	1
f_{004}	148.777	4	1	4	1	4	1	4	1	4	1
f_{041}	158.791	4	0	4	0	4	0	4	0	4	0
f_{022}	172.219	0	0	2	0	0	0	0	0	0	0
		Model I		Model II		Model III		Model IIbis		Model IIIbis	
S^2		2.868		0.373		0.250		0.334		0.203	
$\overline{\Delta X/X}$		0.38%		0.16%		0.13%		0.16%		0.13%	
ΔP		0.455 s		0.189 s		0.159 s		0.214 s		0.168 s	
$T_{\rm eff}$		34,053 K		34,077 K		34,050 K		34,093 K		34,063 K	
log g		5.8047		5.8045		5.8051		5.8127		5.8105	
$M_*/M_\odot$		0.4408		0.4448		0.4470		0.4637		0.4585	
log q(envl)		−4.345		−3.7810		−3.7846		−3.6819		−3.6718	
PFEnvl		3.11		6.54		5.41		4.83		5.21	
log q(core)		−0.3679		−0.3382		−0.3100		−0.1873		−0.2063	
(C+O)		0.920		0.905		0.913		0.815		0.857	
log q(envl,diff)		—		-8.74		-8.63		-7.42		-7.51	
DiffH		—		0.74		0.74		0.66		0.65	
PFDiff		—		1.05		1.18		1.03		1.07	
log q(core, flash)		—		—		-2.61		—		-2.76	
FlashC		—		—		0.07		—		0.07	
PFFlash		—		—		34.3		—		43.5	

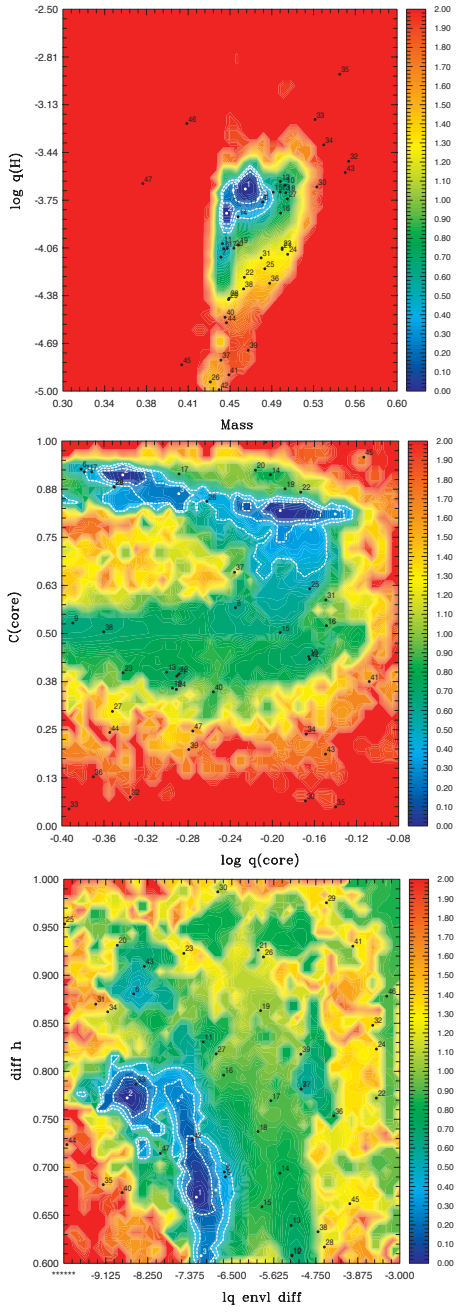

Figure 6. Optimization with 4G models. *Top panel*: map of the projected merit function S^2 (on a logarithmic scale) in the log q(H)–M_* plane. *Middle panel*: map of the projected merit function S^2 (on a logarithmic scale) in the log $q(core)$–$X_{core}(C + O)$ plane. *Bottom panel*: map of the projected merit function S^2 (on a logarithmic scale) in the lqEnvDiff–DiffH plane. Best-fit models are identified by their rank (1 for the lowest merit function, etc. Do not pay attention to solutions with rank higher than 5: the optimization code explores the parameter space until the last iteration, and this simply corresponds to models computed during this last iteration). White contours show regions where the period fits have S^2 values within the 1σ, 2σ and 3σ confidence levels relative to the best-fit solution.

some parameters remains poorly constrained: the profac parameters (PFEnvl, PFDiff, and PFFlash), as well as FlashC and log q(core, flash). This is not a total surprise since the p-modes observed in PG 1219+534 are essentially envelope modes that are largely insensitive to the detailed structure of the deepest regions, and the quality of the fit prevents us from constraining them. The p-modes are also not very sensitive to the exact slope of the transition profiles, although relatively steep envelope transitions (PFEnvl, PFDiff) seem favored. All other parameters show bimodal probability functions, corresponding to the two optimal models identified above. These two models are however similar for most of their parameters, such as the total stellar mass or the C-O core abundance.

In conclusion, including in 4G models a double H/He transition profile in the envelope considerably improves the fit to the observed periods (from $\overline{\Delta X/X}$ = 0.38% to 0.16%), although its precise location (log q(envl, diff)) and the exact H/He mix in the lower envelope (DiffH) is not very accurately constrained. All the parameters related to the potential C-pollution of the He-mantle are practically unconstrained.

4.2.4 Adding *g*-modes

Adding the 6 g-modes to the 9 p-modes led to two very similar optimal models with similar quality of period fit. In other words, the 6 g-modes can easily be integrated in the two optimal models identified above. (As a corollary, they do not help to discriminate between these two solutions). All these modes correspond to high-order g-modes, explaining why these g-modes did not help to constrain further the core or mantle properties, since high-order g-modes have significant amplitudes in the outer regions, as the regions sampled by p-modes. In particular, no interesting further inference of the C-pollution of the He-mantle could be obtained.

4.3 Comparison between 2G, 3G and 4G results

First, let us note that the existence of two optimal 4G models (when considering double H/He transition profile), while only one emerged in 2G, 3G and 5-parameter 4G models is somewhat surprising. This is maybe due to the more exhaustive exploration of the parameter space we carried out when increasing the number of parameters. Actually, the second solution with the smaller core may be guessed in 3G models (Figure 5, right panel), for example.

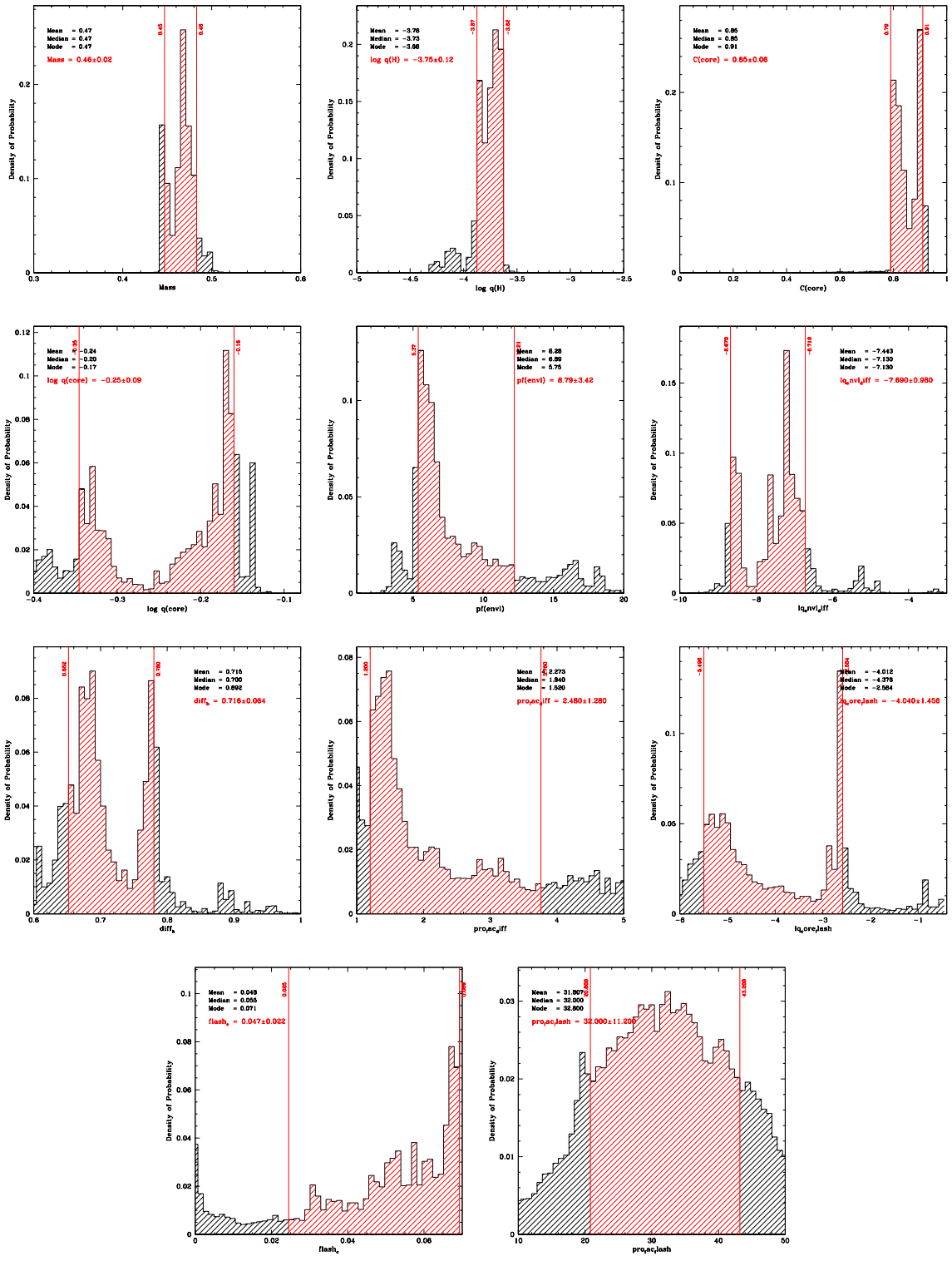

Figure 7. Probability density functions derived from asteroseismology for various parameters of the 4G models. The red-hatched regions between the two vertical solid red lines shows the 1σ range containing 68.3% of the distribution.

Table 3 presents the stellar parameters inferred from seismic fits to the 9 observed p-modes. For 3G and 4G models, the reference value indicated in Table 3 correspond to the central value of the 1σ range of the corresponding probability density functions. This naturally englobes the two optimal solutions for 4G models. All in all, we can affirm that 2G, 3G and 4G models lead to remarkably consistent stellar parameters, corresponding to an sdB with a canonical mass, rather thin H-He envelope, and which is close to He-burning exhaustion.

4.4 Rotation properties of PG 1219+534

In standard pulsation theory (see, *e.g.*, Unno et al. 1979), the spherical harmonics $Y_l^m(\theta, \phi)$ describe the angular dependence of the nonradial oscillation modes. An oscillation eigenmode is characterized by a radial order k, a degree ℓ, and an azimuthal order m. Assuming no stellar rotation, the star is considered spherically symmetric and the frequencies of the oscillation modes are $m \equiv (2\ell + 1)$–fold degenerated. The main effect of stellar rotation on pulsations is to lift this degeneracy, leading to the rotational splitting of nonradial modes into their $2\ell + 1$ components, differing by their m values (with $-\ell \leq m \leq +\ell$). Treated as a perturbation and at the first order of approximation (generally valid for a slowly rotating star), rotation creates groups of evenly spaced multiplets in the frequency domain. Assuming an internal rotation law $\Omega(r)$, the multiplet components are separated by

$$\Delta\nu_{k\ell} = m \int_0^R K_{k\ell}(r)\Omega(r)dr \tag{2}$$

and their frequencies are given by

$$\nu_{k\ell m} = \nu_{k\ell 0} - \Delta\nu_{k\ell} \tag{3}$$

To constrain the rotation of the star, we have to inverse the problem considering the frequency separation $\Delta\nu_{kl}$ and the rotational kernel K_{kl}. The latter, specific to each mode of radial order k and degree ℓ, is defined as

$$K_{k\ell} = \frac{\xi_r^2 + \ell(\ell+1)\xi_h^2 - 2\xi_r\xi_h - \xi_h^2}{\int_0^R (\xi_r^2 + \ell(\ell+1)\xi_h^2)\rho r^2 dr}\rho r^2 \tag{4}$$

where $\xi_r(r)$ and $\xi_h(r)$ are respectively the non-perturbed radial and horizontal displacement eigenfunctions of the mode. From Eq. (2), one can see that the rotational kernel plays the role of weight function and indicates the layers contributing most to the integral giving the frequency spacing between multiplet components.

We used for this proceeding the two multiplet structures associated to the dominant periods f_{002} and f_{003} to probe the internal rotation of PG 1219+534. The doublet $f_{041} - f_{042}$ and the g-mode triplet $f_{012} - f_{016} - f_{020}$ will be considered later. Figure 8 shows the relevant quantities for these two modes from our optimal 3G model of PG 1219+534. To compare properly the kernel distribution associated with one mode with that associated with another mode, we plotted the relative rotation kernels in the upper panel of Figure 8, after having normalized arbitrarily the largest amplitude of all kernels involved with 1. In order to best identify the region over which rotation can be probed, we computed the weighted sum of kernels, which is shown by the dashed curve in the lower subpanel of Figure 8. The region over which the rotation profile can be probed corresponds to those layers where the weighted sum has a non-negligible amplitude. We thus find that rotation can be probed in PG 1219+534 over approximately the outer 40% of its radius. This region encompasses the outer H-rich envelope, but also some part of the He mantle, as illustrated by the chemical stratification of our model shown in the middle panel of Figure 8.

To exploit quantitatively the fine structure caused by rotational splitting in seismic data, we applied the method developed in Charpinet et al. (2008) (see also Giammichele et al. 2016). The method consists in analyzing simultaneously the available rotational data under the assumptions that (1) the star rotates slowly, and (2) it rotates as a solid body. The inferred uniform rotation period, $P_{\rm rot}$, can be used after the fact to verify whether the star indeed rotates slowly, in which case $P_{\rm rot}$ should be much larger than the periods of the pulsation modes of interest and first-order perturbation theory should apply. The hypothesis that the star rotates as a rigid body is next verified through stringent tests. Under the a priori assumption that PG 1219+534 spins slowly and rigidly, the optimization problem is a simple 1D exercise featuring the behavior of the merit function[4]:

$$S^2 = \sum_{i=1}^{N_{\rm obs}} \left(\frac{\Delta\nu_{\rm obs}^{(i)} - \Delta\nu_{\rm th}^{(i)}}{\sigma_{\rm obs}^{(i)}} \right)^2 \tag{5}$$

where $\Delta\nu_{\rm obs}^{(i)}$ is the i-th observed frequency spacing between two rotationally split components within a multiplet, $\sigma_{\rm obs}$ its associated uncertainty, and $\Delta\nu_{\rm th}^{(i)}$ is the theoretical spacing for the same two components computed from Eq. (2) assuming solid-body rotation. We have $N_{\rm obs} = 4$ for PG 1219+534. Minimizing this merit function, the rotational data are best explained globally with a value of

4 This merit function should not to be confused with the merit function above related to period matching.

Table 3. Global and internal parameters of PG 1219+534 derived from spectroscopy and asteroseismology.

Quantity	Spectroscopy	Asteroseismology		
	Misc. (see Sect. 2)	2G model (Charpinet et al. 2005)	3G model (this study)	4G model (this study)
$T_{\rm eff}$ (K)	34 258 ± 170	33 640 ± 1360	33 840 ± 225	34225 ± 193
log g	5.838 ± 0.030	5.8071 ± 0.0057	5.806 ± 0.002	5.8044 ± 0.0042
log N(He)/N(H)	−1.475 ± 0.030	...	...	...
$M_*/M_\odot$	...	0.457 ± 0.007	0.439 ± 0.004	0.46 ± 0.02
log($M_{\rm env}/M_*$)	...	−4.254 ± 0.137	−4.32 ± 0.08	−3.75 ± 0.12
log($M_{\rm core}/M$*)	...	...	−0.31 ± 0.01	−0.25 ± 0.09
$X_{\rm core}(C+O)$	...	...	0.91 ± 0.02	0.85 ± 0.06
PF(envl)	...	...	...	8.79 ± 3.42
log q(envl,diff)	...	...	...	−7.69 ± 0.98
H(diff)	...	...	...	0.716 ± 0.064
PF(diff)	...	...	...	2.48 ± 1.28
PF(flash)	...	...	...	32.0 ± 11.2
log q(core,flash)	...	...	...	−4.040 ± 1.456
C(flash)	...	...	...	0.047 ± 0.022

the rotation period $P_{\rm rot}$= 837.87 ± 20.17 h (i.e., 34.91 ± 0.84 days). The result of the minimization is shown in the upper panel of Figure 9. Not surprisingly, this value confirms that PG 1219+534 rotates very slowly, with a rotation period much larger than the pulsation periods, and the first-order perturbative theory fully applies.

We next test the hypothesis of solid body rotation (at least in the region where the weighted sum of the rotation kernels has a non-negligible amplitude) by testing a variable step rotation law. We suppose that the star is divided into two zones, an inner one assumed to rotate rigidly with a period P_i that may be varied, and an outer one assumed to rotate rigidly with the fixed uniform period $P_{\rm rot}$. The location of the transition between the two zones is allowed to freely vary from the center to the surface on a normalized radius scale, r/R. The 2D merit function S^2 must now be optimized as a function of P_i and r/R. Hence, if PG 1219+534 rotates as a rigid body, the merit function must show a minimum when $P_i = P_{\rm rot}$, irrespective of the depth r/R. This is exactly the result the lower panel of Figure 9 illustrates, at least down to depths beyond which the method loses its sensitivity owing to the fact that the amplitudes of the rotation kernels plunge to very small values.

In conclusion, PG 1219+534 rotates extremely slowly and as a solid body at least from $0.6R_*$ to the surface. How this compares to other sdB stars, and to white dwarf progenies, is discussed in Charpinet et al. (these proceedings).

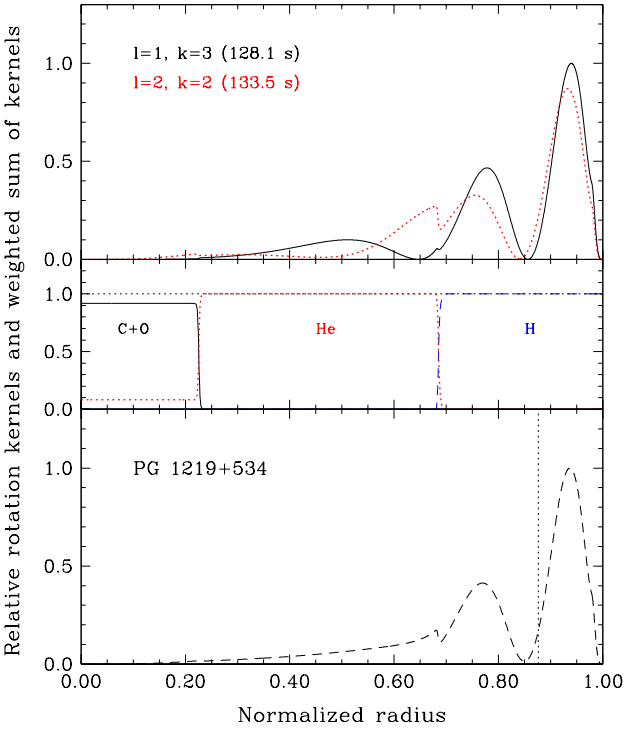

Figure 8. *Top panel*: Relative rotational kernels $K_{k\ell}$ as a function of normalized radius for the two multiplet structures associated to 128.1 s and 133.5 s periods observed in the light curve of PG1219+534. *Middle panel:* Chemical stratification of the model. *Bottom panel:* Weighted sum of the kernels versus normalized radius. The vertical dotted line defines the layer where half of the running integral of the weighted sum is below and the other half above.

5 Conclusion

In this paper we presented a new asteroseismic analysis of the sdB pulsator PG 1219+534, based on improved atmospheric parameters from new spectroscopic observations and improved atmospheric modeling, new photometric observations by a 3-month campaign carried out at Mt Bigelow (Arizona), and by using our 3G and 4G sdB models. We obtained very consistent results between various analyses with the third and fourth generation of sdB models, and also with previously published analysis with second generation sdB models. It corresponds to a sdB with a canonical mass (0.46 ± 0.02 $M_{\odot}$), rather thin H-He envelope (log q(envl)= −3.75 ± 0.12), and close to He-burning exhaustion ($X_{\rm core}(C + O)$ = 0.86 ± 0.05). We also investigate the internal rotation of the star. We find that PG 1219+534 rotates very slowly ($P_{\rm rot}$= 34.91 ± 0.84 days) and that solid-body rotation is reached at least down to 0.6$R_{\star}$, encompassing the H-rich envelope and part of the He mantle of the star.

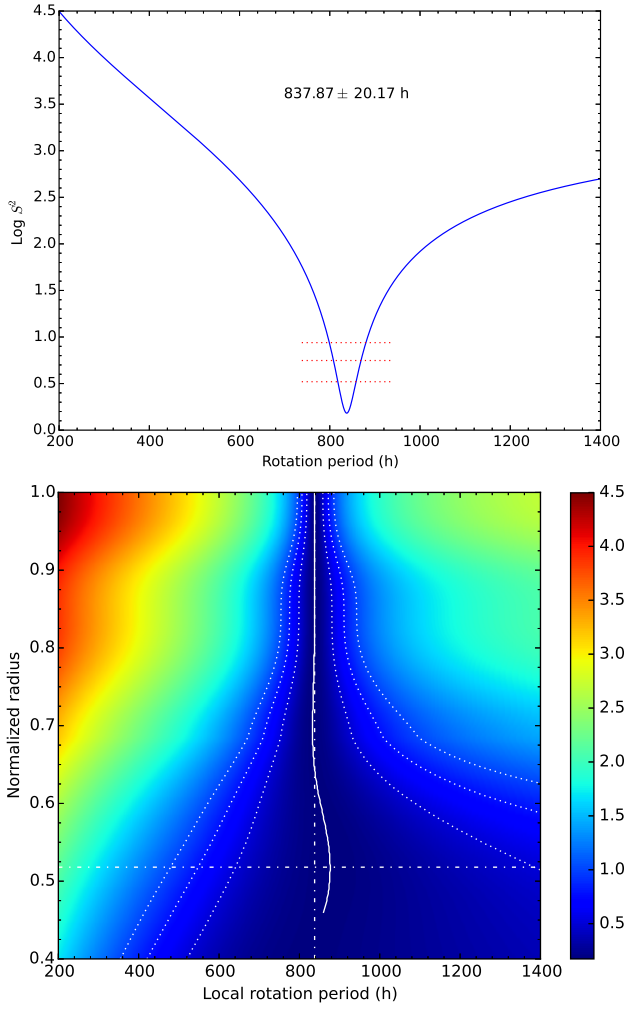

Figure 9. *Top panel:* Result of the optimization procedure under the hypothesis that PG 1219+534 rotates slowly and rigidly. This shows the behavior of the merit function S^2 in terms of the assumed rotation period. The dotted horizontal lines correspond, from bottom to top, to the 1-, 2-, and 3-σ limits. *Bottom panel:* Result for solid-body rotation using a variable step rotation law. This is a contour map indicating the behavior of the 2D merit function S^2 as a function of depth (expressed in fractional radius) and in terms of the rotation period of the inner region of our two-zone approach. The solution is illustrated by the nearly vertical white curve and the dotted white curves depicting its associated 1-, 2-, and 3-σ contours. These contours diverge out at large depths which indicates that the rotationally split p-modes available in the present case lose their capacity to measure the local rotation rate there. The horizontal dot-dashed line indicates the layer above which there is 1% of the mass of the star.

References

Blanchette, J.-P., Chayer, P., Wesemael, F., Fontaine, G., Fontaine, M., Dupuis, J. et al. 2008, ApJ, 678, 1329–1341.
Charpinet, S., Fontaine, G., Brassard, P., & Dorman, B. 1996, ApJ, 471, L103–106.
Charpinet, S., Fontaine, G., Brassard, P., Chayer, P., Rogers, F. J., Iglesias, C. A. et al. 1997, ApJ, 483, L123–L126.
Charpinet, S., Fontaine, G., Brassard, P., Green, E. M., & Chayer, P. 2005, A&A, 437, 575–597.
Charpinet, S., Van Grootel, V., Reese, D., Fontaine, G., Green, E. M., Brassard, P. et al. 2008, A&A, 489, 377-394.
Charpinet, S., Van Grootel, V., Fontaine, G., Green, E. M., Brassard, P., Randall, S. K. et al. 2011, A&A, 530, A3.
Dorman, B., Rood, R. T., & O'Connell, R. W. 1993, ApJ, 419, 596–614.
Fontaine, G., Brassard, P., Charpinet, S., Green, E. M., Chayer, P., Billéres, M. et al. 2003, ApJ, 597, 518–534.
Giammichele, N., Fontaine, G., Brassard, P., & Charpinet, S. 2016, ApJS, 223, 10.
Giammichele, N., Charpinet, S., Brassard, P. & Fontaine, G. 2017, A&A, 598, A109.
Han, Z., Podsiadlowski, P., Maxted, P. F. L., Marsh, T. R., & Ivanova, N. 2002, MNRAS, 336, 449-466.
Han, Z., Podsiadlowski, P., Maxted, P. F. L., & Marsh, T. R. 2003, MNRAS, 341, 669–691.
Koen, C., O'Donoghue, D., Pollacco, D. L., & Charpinet, S. 1999, MNRAS, 305, 28–38.
Randall, S. K., Fontaine, G., Brassard, P., & Bergeron, P. 2005, ApJS, 161, 456–479.
Tremblay, P.-E., Fontaine, G., Brassard, P., Bergeron, P., & Randall, S. K. 2006, ApJS, 165, 551–567.
Unno, W., Osaki, Y., Ando, H., & Shibahashi, H. 1979, Nonradial oscillations of stars, University of Tokyo Press, Japan.
Van Grootel, V., Charpinet, S., Fontaine, G., Brassard, P., Green, E. M., Chayer, P. et al. 2008, A&A, 488, 685–696.
Van Grootel, V., Charpinet, S., Brassard, P., Fontaine, G., & Green, E. M. 2013, A&A, 553, A97.